



# Extraction of tissue optical property and blood flow from speckle contrast diffuse correlation tomography (scDCT) measurements

MINGJUN ZHAO,  CHONG HUANG, SIAVASH MAZDEYASNA, AND GUOQIANG YU\*

University of Kentucky, Department of Biomedical Engineering, Lexington, Kentucky 40506, USA

\*guoqiang.yu@uky.edu

**Abstract:** Measurement of blood flow in tissue provides vital information for the diagnosis and therapeutic monitoring of various vascular diseases. A noncontact, camera-based, near-infrared speckle contrast diffuse correlation tomography (scDCT) technique has been recently developed for 3D imaging of blood flow index ( $\alpha D_B$ ) distributions in deep tissues up to a centimeter. A limitation with the continuous-wave scDCT measurement of blood flow is the assumption of constant and homogenous tissue absorption coefficient ( $\mu_a$ ). The present study took the advantage of rapid, high-density, noncontact scDCT measurements of both light intensities and diffuse speckle contrast at multiple source-detector distances and developed two-step fitting algorithms for extracting both  $\mu_a$  and  $\alpha D_B$ . The new algorithms were tested in tissue-simulating phantoms with known optical properties and human forearms. Measurement results were compared against established near-infrared spectroscopy (NIRS) and diffuse correlation spectroscopy (DCS) techniques. The accuracies of our new fitting algorithms with scDCT measurements in phantoms (up to 16% errors) and forearms (up to 23% errors) are comparable to relevant study results (up to 25% errors). Knowledge of  $\mu_a$  not only improved the accuracy in calculating  $\alpha D_B$  but also provided the potential for quantifying tissue blood oxygenation via spectral measurements. A multiple-wavelength scDCT system with new algorithms is currently developing to fit multi-wavelength and multi-distance data for 3D imaging of both blood flow and oxygenation distributions in deep tissues.

© 2021 Optical Society of America under the terms of the [OSA Open Access Publishing Agreement](#)

## 1. Introduction

Blood flow (BF) facilitates the delivery of nutrients and oxygen to tissues and removal of metabolic byproducts from tissues. Continuous monitoring of BF in tissue provides information to medical professionals for the diagnosis and therapeutic monitoring of various diseases associated with tissue ischemia, such as peripheral arterial disease, cerebral vascular disease, and various types of wounds [1,2]. Tissue oxygenation level, on the other hand, reflects the balance between oxygen supply (via BF) and oxygen consumption, and thus is an important biomarker for tissue hypoxia associated with tissue injury [3,4]. Furthermore, simultaneous monitoring of BF and tissue oxygenation allows for the estimation of tissue oxygen consumption, another crucial biomarker for tissue pathophysiological conditions [3–5].

A wide range of imaging technologies have been developed for the assessment of tissue hemodynamics and metabolism, including magnetic resonance imaging (MRI) [6], positron emission tomography (PET) [7], single photon emission computed tomography (CT) [8], and xenon CT [9]. However, these large imaging modalities are expensive and difficult to use for continuous and longitudinal monitoring. By contrast, optical instruments are portable, inexpensive, continuous, and fast [10–21]. Near-infrared/diffuse correlation spectroscopy (NIRS/DCS) and corresponding diffuse optical/correlation tomography (DOT/DCT) technologies use continued point illumination and discrete photodetectors to detect deep tissue hemodynamics (up to several

centimeters) [4,22–36]. Conventional NIRS/DOT measures light intensity attenuations by tissue absorption and scattering at multiple wavelengths ( $\lambda$ ). The oxy- and deoxy-hemoglobin concentrations are calculated from the measured tissue absorption coefficient  $\mu_a(\lambda)$  [5,36]. The relatively new DCS/DCT uses coherent point illumination and single-photon-counting avalanche photodiode detection of temporal fluctuations of diffuse speckles for BF measurements. Although effective, these optical systems employ limited numbers of sources and detectors, thus lacking the combination of high temporal-spatial resolution and wide field-of-view (FOV) to image spatially distributed tissue hemodynamics.

Use of a remote wide field illumination and 2D detection by a charge-coupled device (CCD) or complementary metal-oxide-semiconductor (CMOS) camera achieves fast, high-resolution, 2D mapping of tissue hemodynamics in a noncontact manner. For example, conventional laser speckle contrast imaging (LSCI) [16,17,37] and optical intrinsic signal imaging (OISI) [38] enable noncontact 2D mapping of blood flow and oxygenation distributions, respectively. However, both LSCI and OISI are mainly sensitive to the tissue surface with limited penetration depths ( $< 1$  mm), therefore they are inadequate for noninvasive imaging of deep tissues hemodynamics.

Our group recently developed a noncontact, camera-based, speckle contrast diffuse correlation tomography (scDCT) technique for 3D imaging of BF distributions in deep tissues [39–47]. In contrast to 2D surface mapping techniques (LSCI and OISI) with a wide-field illumination, scDCT remotely scans point, coherent near-infrared light via a galvo mirror to multiple source positions, thus enabling a deeper tissue penetration (up to  $\sim 10$  mm). scDCT employs a sensitive scientific CMOS (sCMOS) camera to detect spatial diffuse speckle fluctuations resulting from moving red blood cells in the microvasculature (i.e., tissue BF). The fully noncontact data acquisition with adjustable source-detector (S-D) configuration over a flexible region-of-interest (ROI) enables rapid, high-density, 3D imaging of BF distributions. In a recent portable scDCT system, all electrical and optical parts are assembled into a mobile cart ( $23 \times 23 \times 41$  cubic inches, TCP23FF, Bretford, IL). scDCT system has been tested for 3D imaging of blood flow distributions in animal brains (mice, rats, piglets) and human tissues (infant brains, wound/burned tissues, mastectomy skin flaps) [39–47]. In some of these studies, scDCT was compared with other established methods including laser Doppler, DCS, and fluorescence angiography; consistent results were observed among these methods in detecting BF variations.

A limitation with continuous-wave measurements of BF is the assumption of constant and homogenous  $\mu_a(\lambda)$  and  $\mu'_s(\lambda)$  (reduced scattering coefficient) from the literature [48–50]. Although this assumption is widely accepted in DCS/DCT, inter-subject heterogeneity and potential dynamic variations in  $\mu_a(\lambda)$  and  $\mu'_s(\lambda)$  may cause errors in calculating BF variations [51–54]. It has been shown that fitting DCS data of auto-correlation functions ( $g_1$ ) at multiple S-D distances and multiple wavelengths enables simultaneous extractions of  $\mu_a(\lambda)$ ,  $\mu'_s(\lambda)$  and blood flow index (BFI) for a homogeneous tissue volume [51]. Because of the intrinsic relationship between diffuse speckle contrast and auto-correlation function, it is possible to extract BFI and optical properties from diffuse speckle contrast measurements at multiple S-D distances and/or at multiple exposure times. For example, Valdes et al. performed speckle contrast optical spectroscopy measurements at multiple S-D distances (5 to 20 mm with an increment of 2.5 mm) to quantitatively fit for BFIs in tissue-simulating phantoms and human forearms [53]. Similarly, Dragojevic et al. conducted speckle contrast optical tomographic reconstructions with multiple S-D distances (up to 6.5 mm) for quantification of BFIs in rodent's brains [55,56]. More recently, Liu et al. explored extracting  $\mu_a(\lambda)$ ,  $\mu'_s(\lambda)$ , coherence factor ( $\beta$ ), and BFI from diffuse speckle contrast analysis at multiple S-D distances (2.5 to 10.5 mm with an incremental step of 1 mm) and with multiple exposure times (0.1 to 1 ms with an increment of 0.1 ms) [52]. The spectroscopic measurements (not imaging) were made in a semi-contact manner with a source fiber in contact with the tissue phantom. The fitting accuracy depended highly on data quality, which required long-time data acquisition and averaging: 1000 frames at each exposure time. Their system was

tested in tissue phantoms with known optical properties and data acquisition time was tens of minutes for each step of multi-distance and multi-exposure measurements [52].

To overcome the limitations of existing systems, we took the advantage of rapid, high-density, noncontact scDCT measurements of both light intensities and diffuse speckle contrasts at multiple S-D distances and developed new algorithms for extracting both  $\mu_a(\lambda)$  and  $BFI$ . The noncontact hardware of scDCT makes data acquisition easy and fast with a high sampling density. scDCT usually scans a point light via an electronically-controlled galvo mirror (switching time: 1 ms) to multiple source positions and takes one or more images by the sCMOS camera at each source position with a single exposure time of a few milliseconds per image [40–47]. The fast and high-density sampling by the sCMOS camera sensor array (e.g.,  $2048 \times 2048$  pixels) enables rapid tomographic imaging of tissue hemodynamic distributions with improved signal-to-noise ratio (SNR) (via spatial data averaging) [39–46]. The optimized scDCT acquires one scanning over multiple source positions (e.g.,  $9 \times 9$ ) within  $\sim 1.5$  minutes with numerous S-D pairs at larger distances up to 20 mm, which benefits larger penetration depths.

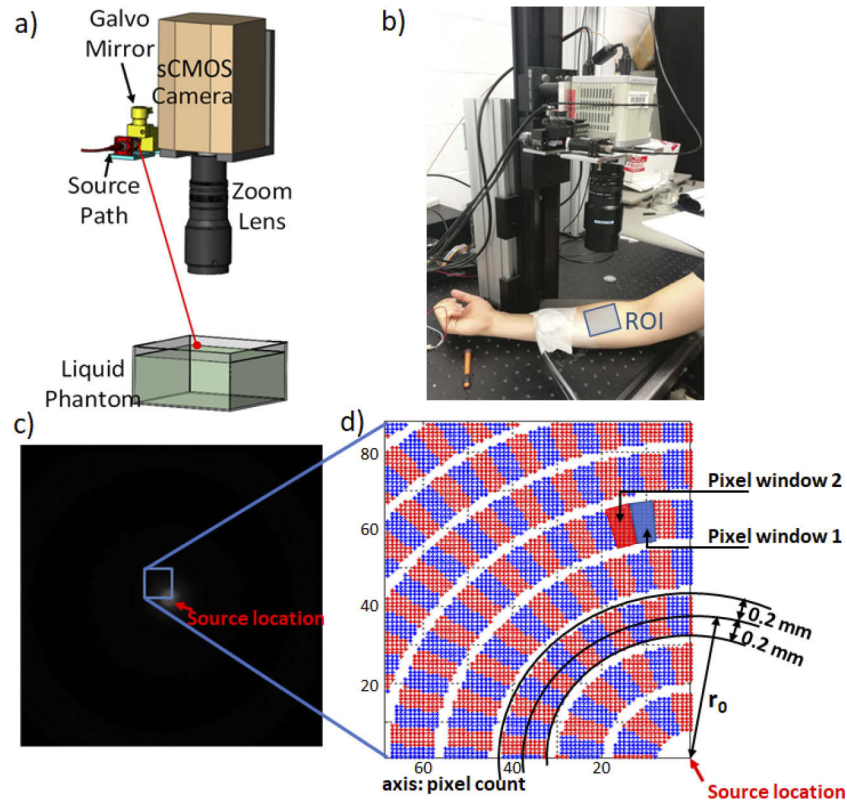


**Fig. 1. scDCT Measurement Setup and Pixel-window Definition.** (a) In the phantom test, a long coherence laser is connected to the galvo mirror through a multimode optical fiber. The galvo mirror projects the point light to the center of the liquid phantom. A sCMOS camera is used to capture the intensity image in a selected region of interest (ROI). (b) In the *in-vivo* test, scDCT is used to collect the data from the ROI on human forearm. (c) An illustrative raw intensity image taken from the selected ROI. The point source locates at the center of ROI. (d) A zoom-in view of a small area around the source. A pixel-window at the S-D distance of  $r_0$  is defined in a cluster with adjacent 50 pixels marked with the same color (blue or red). Note that pixel windows in all directions around the source  $r_0$  are used for data analysis.

The focus of the present study was to demonstrate the feasibility and accuracy of our new two-step fitting algorithms for the extraction of both  $\mu_a$  and  $\alpha D_B$  from scDCT measurements. Therefore, only one source located at the center of the ROI was used in this study for proof of the concept. Data acquisition time at one source position was less than 10 seconds. The new fitting algorithms were tested in tissue-simulating phantoms with known optical properties and human forearms. Measurement results were compared against established NIRS/DCS techniques. Knowledge of  $\mu_a(\lambda)$  not only improved the accuracy in calculating *BFI* but also provides the potential for quantifying tissue blood oxygenation via spectral measurements [36,57,58]. As mentioned earlier, oxygenation information can be determined by measuring  $\mu_a(\lambda)$  at multiple wavelengths using NIRS principles.

## 2. Methods

### 2.1. scDCT system

Details about the patented scDCT are described elsewhere [39–47]. In the scDCT (Fig. 1(a) and Fig. 1(b)), a point-source coherent light at 830 nm generated from a long-coherence laser (Crystalaser, NV) was coupled through a multimode fiber (core size: 200 microns) to an achromatic lens (AC127-019-B, Thorlabs, NJ) and a galvo mirror (GVS002, Thorlabs, NJ). The galvo mirror projected light to desired source positions over a selected ROI. In this study, a single source position located at the center of the ROI was used to test our new algorithms (Fig. 1(c)).

A sCMOS camera (Orca Flash 4.0LT, Hamamatsu, Japan) was used for data collection at 25 frames per second. A zoom lens (Zoom 7000, Navitar, NY) was mounted to the camera enabling easy adjustment of ROI and F number. The camera detected diffuse light from the tissue surface in a reflectance mode with a typical exposure time of 2 ms. A pair of polarizers (LPNIRE050-B and LPNIRE200-B, Thorlabs, NJ) were added across the source and detection paths to reduce direct reflection from sources. A long-pass filter ( $> 800$  nm, 84-762, Edmund Optics, NJ) was added in front of the zoom lens to minimize the influence of ambient light.

The speckle contrast is defined as:

$$K_s(\mathbf{r}) = \frac{\sigma_s}{\langle I \rangle} \quad (1)$$

Here,  $\sigma_s$  and  $\langle I \rangle$  are the spatial standard deviation and mean value of light intensities over a pixel window of 50 pixels, respectively (Fig. 1(d)).  $\mathbf{r}$  is the distance between the centers of the pixel-window and source. The diffuse speckle contrast  $K_s(\mathbf{r})$  can be related to the temporal auto-correlation function  $g_1(\mathbf{r}, \tau)$  via the following equation [39]:

$$K_s^2(\mathbf{r}) = \frac{2\beta}{T} \int_0^T \left(1 - \frac{\tau}{T}\right) [g_1(\mathbf{r}, \tau)]^2 d\tau \quad (2)$$

Here,  $T$  is the exposure time and  $\tau$  is the correlation lag time. By substituting  $g_1(\mathbf{r}, \tau)$  with its analytical solution in semi-infinite geometry, a nonlinear relationship between  $K_s(\mathbf{r})$  and the *BFI* ( $\alpha D_B$ ) was derived in our previous publication [39].  $K_s(\mathbf{r})$  can be then written as a function of  $\alpha D_B$ , together with other parameters:

$$K_s^2(\mathbf{r}) = f(\alpha D_B, T, \mu_a(\lambda), \mu'_s(\lambda), \lambda, \beta, k_0, \mathbf{r}) \quad (3)$$

Here,  $\lambda$  is the wavelength of the source,  $\beta$  is the coherence factor, and  $k_0$  is the wavenumber.  $\alpha D_B$  is a combined term representing *BFI*, where  $\alpha$  is a unitless ratio of dynamic scatterers to total scatterers and  $D_B$  (unit:  $\text{cm}^2/\text{s}$ ) is the effective diffusion coefficient of moving scatterers.

### 2.2. New algorithms for extracting $\mu_a$ and $\alpha D_B$

As  $K_s(\mathbf{r})$  is a function of multiple parameters including  $\alpha D_B$ ,  $\mu_a(\lambda)$  and  $\mu'_s(\lambda)$  Eq. (3), assumptions of optical properties ( $\mu_a(\lambda)$  and  $\mu'_s(\lambda)$ ) from literature may lead to errors in  $\alpha D_B$  calculations.

Thus, a new approach with two fitting steps is proposed here to extract both  $\mu_a$  and  $\alpha D_B$  from scDCT measurements: (1)  $\mu_a(\lambda)$  is extracted by fitting the measured light intensities ( $I$ ) at multiple S-D distances (Fig. 2(a)) and (2)  $\alpha D_B$  is assessed by fitting the measured speckle contrasts ( $K_s(\mathbf{r})$ ) at multiple S-D distances (Fig. 2(b)) with the input of known  $\mu_a(\lambda)$  obtained from the first step. The influence of  $\mu'_s(\lambda)$  assumption is discussed in Section 4.

In the first step, the simplified solution of photon diffusion equation is given by [54,59,60]:

$$\ln [I(\mathbf{r}) r^2] = I(\mathbf{r} = 0) - r \mu_{eff} \quad (4)$$

Here,  $I(\mathbf{r})$  is the light intensity measured at the S-D separation  $\mathbf{r}$ , and  $\mu_{eff}$  is the effective attenuation coefficient defined as:

$$\mu_{eff}(\lambda) = \sqrt{3 \mu_a(\lambda) \cdot \mu'_s(\lambda)} \quad (5)$$

Based on Eq. (4),  $\ln [I(\mathbf{r}) r^2]$  has a linear relationship with  $\mathbf{r}$  [54,59,60]. Thus,  $\mu_{eff}(\lambda)$  can be extracted by fitting the slope of logarithmic light intensities over multiple S-D separations. By assuming  $\mu'_s(\lambda)$  from literature or acquiring  $\mu'_s(\lambda)$  from other measurements,  $\mu_a(\lambda)$  can be calculated from  $\mu_{eff}(\lambda)$  (Fig. 2(a)) [48–50].

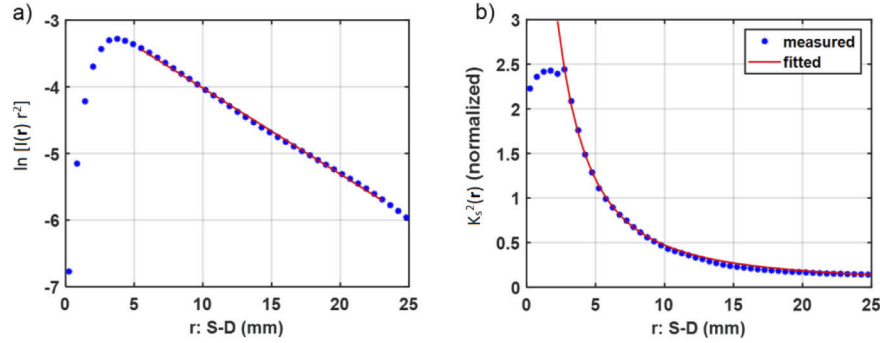


**Fig. 2. A Two-step Approach for Extraction of  $\mu_a$  and  $\alpha D_B$ .** (a) Fitting the effective attenuation coefficient ( $\mu_{eff}$ ) from the light intensities  $I(\mathbf{r})$  measured at multiple S-D distances. (b) Fitting blood flow index ( $\alpha D_B$ ) from  $K_s^2(\mathbf{r})$ , measured at multiple S-D distances.

The second step is to fit  $\alpha D_B$  from the measured speckle contrasts at multiple S-D distances by minimizing the penalty term [52,53,61,62]:

$$\chi^2 = \sum_{i=1}^{N_r} [K_m^2(r_i, \alpha D_B) - K_t^2(r_i, \alpha D_B)]^2 \quad (6)$$

Here,  $K_m^2$  is the experimentally measured speckle contrasts and  $K_t^2$  is the theoretical speckle contrasts with an initial guess of  $\alpha D_B$ , calculated using Eq. (3). To eliminate the influence of linear scaling factor  $\beta$  in Eq. (3), both  $K_m^2$  and  $K_t^2$  are normalized to their mean values over all the selected  $\mathbf{r}$ , respectively (Fig. 2(b)). The normalization cancels the constant  $\beta$  from calculations [21,53].

Since there is only one wavelength ( $\lambda = 830 \text{ nm}$ ) involved in the experiments in this work, we write  $\mu_a(\lambda)$  and  $\mu'_s(\lambda)$  as  $\mu_a$  and  $\mu'_s$  from here on for simplicity.

### 2.3. Phantom tests with varied $\mu_a$ and $\alpha D_B$

To examine performance of the new algorithms, tissue-like liquid phantom tests were first performed (Fig. 1(a)). A glass tank was filled with a liquid solution that consisted of distilled



water, India ink (Black India, MA) and Intralipid (Fresenius Kabi, Sweden) [40,63].  $\mu_a$  and  $\alpha_{DB}$  were varied via ink titration and temperature variation of the liquid phantom, respectively. A FOV of  $90 \times 90 \text{ mm}^2$  was selected in the phantom center for scDCT measurements, with a single source position fixed in the center of the FOV (Fig. 1(c)). Camera exposure time was set as 2 ms and F# was 8. At each level of  $\mu_a$  and  $\alpha_{DB}$ , 50 frames were taken by scDCT within 2 seconds for averaging to improve SNR.

For comparison purpose,  $\mu_a$  and  $\alpha_{DB}$  were also measured using an established hybrid instrument combining a commercial NIRS device (Imagent, ISS, IL) for  $\mu_a$  and a customized DCS device for  $\alpha_{DB}$  [57,58,63,64]. NIRS and DCS data were taken by a hybrid fiber-optic probe placing on the phantom surface immediately after scDCT measurement at each step.

Ink titration to change  $\mu_a$ .  $\mu'_s$  and  $\alpha_{DB}$  were set up and kept as  $10.2 \text{ cm}^{-1}$  and around  $1.15 \times 10^{-8} \text{ cm}^2/\text{s}$  throughout titration steps. Indian ink was added step-by-step to create gradient increases in  $\mu_a$  ( $\lambda = 830 \text{ nm}$ ) from  $0.04 \text{ cm}^{-1}$  to  $0.16 \text{ cm}^{-1}$  with  $0.03 \text{ cm}^{-1}$  increment per step. At each titration step, the phantom was stirred thoroughly and then rested for 2 minutes to allow for stabilization before data collection by scDCT and NIRS/DCS.

Temperature variation to change  $\alpha_{DB}$ .  $\mu_a$  and  $\mu'_s$  were set up and kept as  $0.1 \text{ cm}^{-1}$  and  $10.2 \text{ cm}^{-1}$  ( $\lambda = 830 \text{ nm}$ ), respectively, during temperature changes to create  $\alpha_{DB}$  variations. Brownian motions of Intralipid particles ( $\alpha_{DB}$ ) were varied via temperature changes of the phantom from  $\sim 5^\circ\text{C}$  (fridge temperature) to  $\sim 25^\circ\text{C}$  (room temperature). Data were collected at each increment of  $5^\circ\text{C}$  using scDCT and NIRS/DCS devices, sequentially. Phantom temperature was continuously monitored by a thermometer throughout the test.

#### 2.4. In-vivo tests in human forearms

To validate new algorithms for *in-vivo* tests, resting baseline measurements were performed in five human forearms. This study was approved by the University of Kentucky Institutional Review Board. The subject's forearm was secured on a table with an arm support (Fig. 1(b)). A FOV of  $60 \times 60 \text{ mm}^2$  was selected to adapt to the dimensions of forearm, while other settings were kept the same as in the phantom tests. In total, 250 frames were taken by noncontact scDCT within 10 seconds from the resting forearm. For comparison purpose,  $\mu_a$  and  $\alpha_{DB}$  were then measured by a contact hybrid NIRS/DCS probe placing on the same area.

#### 2.5. Data analysis

Dark noise and shot noise were first removed from the raw scDCT images using the methods reported previously [39–46]. Spatial speckle contrasts  $K_s(\mathbf{r})$  and light intensities at all directions around the source were calculated (Fig. 1(d)). Different ranges of S-D distances were used for data analysis to adapt different sizes of FOV: 0.25 to 35 mm for phantoms and 0.25 to 20 mm for human forearms, with an increment of 0.5 mm. For each S-D distance  $r_0$ , all pixels within the distance range of  $(r_0 - 0.2) \text{ mm} \leq r \leq (r_0 + 0.2) \text{ mm}$  around the source were selected and segmented into pixel windows consisted of 50 adjacent pixels (Fig. 1(d)). The speckle contrast  $K_s(\mathbf{r})$  at each pixel window was calculated using Eq. (1). After excluding 50% outlier data (the highest and lowest 25%), light intensities and speckle contrasts at  $r_0$  were then averaged to obtain mean values of  $I(r_0)$  and  $K_s(r_0)$ , respectively. Note that the outlier data removal is primarily used to reduce the influence of spatial *in-vivo* tissue heterogeneity. In addition to the spatial averaging, time-course data of  $I(r_0)$  and  $K_s(r_0)$  were averaged over 50 frames to further improve SNRs.

Based on experimental results (see Section 3), effective S-D distances were determined for extracting  $\mu_a$  and  $\alpha_{DB}$  using the two-step fitting algorithms Eq. (4)–(6). A constant  $\mu'_s$  was set up in all tissue phantoms based on the phantom recipe, while  $\mu'_s$  values in human forearms were measured by the commercial NIRS device (Imagent).

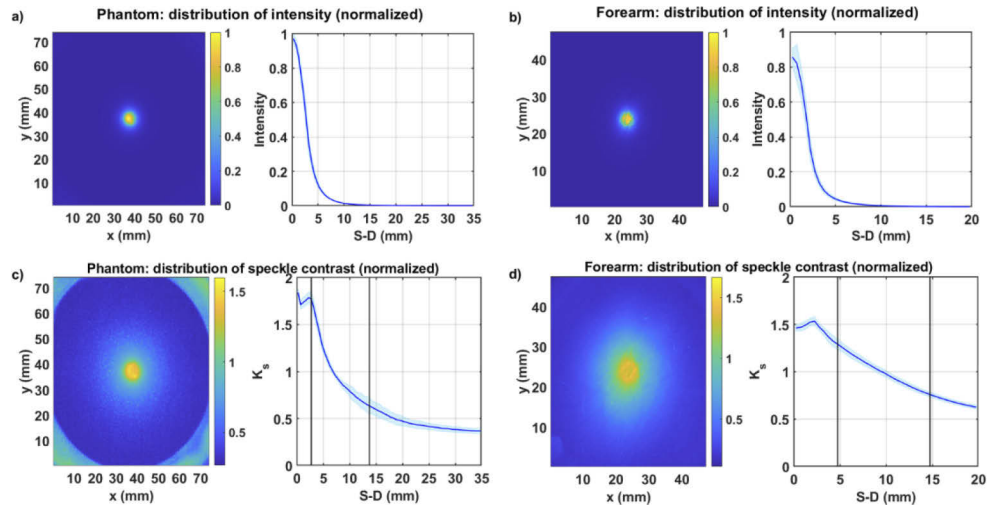
The results from scDCT and NIRS/DCS measurements were compared and percentage errors were calculated by taking NIRS/DCS measurements as standards. Linear regressions were

conducted and Pearson correlation coefficients were calculated to evaluate correlations between the scDCT and NIRS/DCS measurements. Paired t-tests were used to test group differences between the two measurements.  $p < 0.05$  was considered a statistically significant correlation between the two measurements.

### 3. Results

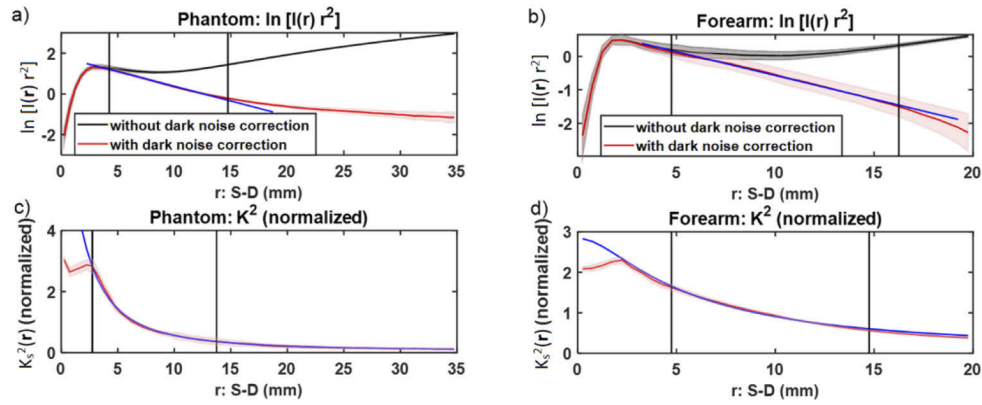
#### 3.1. Determination of effective S-D distances for extracting $\mu_a$ and $\alpha D_B$

Figure 3 shows typical distributions of light intensities (**a** and **b**) and speckle contrasts (**c** and **d**), measured from a liquid phantom ( $\mu_a = 0.1 \text{ cm}^{-1}$ ,  $\mu'_s = 10.2 \text{ cm}^{-1}$ , and  $\alpha D_B = 1.28 \times 10^{-8} \text{ cm}^2/\text{s}$ , **a** and **c**) and a human forearm ( $\mu_a = 0.25 \text{ cm}^{-1}$ ,  $\mu'_s = 5.3 \text{ cm}^{-1}$ , and  $\alpha D_B = 0.79 \times 10^{-8} \text{ cm}^2/\text{s}$ , **b** and **d**). For visualization and comparison,  $I(\mathbf{r})$  data were normalized to the source location ( $\mathbf{r} = 0 \text{ mm}$ ) and  $K_s^2(\mathbf{r})$  data were normalized to the mean value of  $K_s^2(\mathbf{r})$  in the selected effective S-D ranges. Although variations existed, data from the phantom and human forearm had similar patterns.



**Fig. 3. Typical Distributions of Light Intensities (Top) and Speckle Contrasts (Bottom) in a Phantom (Left) and a Human Forearm (Right).** Data in each subfigure are presented as spatially distributed images around the source (left) and functional curves (mean  $\pm$  standard deviation) against S-D distance (right). After dark noise correction, light intensities were normalized to the source location (i.e., S-D distance = 0) and speckle contrasts were normalized to the mean value of speckle contrasts in the effective S-D range between the two vertical lines. The phantom properties (measured by the NIRS/DCS device):  $\mu_a = 0.1 \text{ cm}^{-1}$ ,  $\mu'_s = 10.2 \text{ cm}^{-1}$ , and  $\alpha D_B = 1.28 \times 10^{-8} \text{ cm}^2/\text{s}$ . The human forearm properties (measured by the NIRS/DCS device):  $\mu_a = 0.25 \text{ cm}^{-1}$ ,  $\mu'_s = 5.3 \text{ cm}^{-1}$ , and  $\alpha D_B = 0.79 \times 10^{-8} \text{ cm}^2/\text{s}$ .

Figure 4 demonstrates that noise corrections significantly improved the linearities of  $\ln [I(\mathbf{r}) r^2]$ , thus extending effective S-D ranges for the phantom (**a**) and forearm (**b**), respectively. The effective S-D ranges were empirically determined based on satisfactory of data fitting in  $\ln [I(\mathbf{r}) r^2]$  (**a** and **b**) and  $K_s^2(\mathbf{r})$  (**c** and **d**) to the models Eq. (4)–(6), respectively. Based on our measurement results from all tissue phantoms and human forearms, effective S-D ranges used in this study were determined and listed in Table 1.



**Fig. 4. Dark Noise Correction and Effective S-D Range Determination.** (a) and (b) Comparison of  $\ln[I(r)r^2]$  (mean  $\pm$  standard deviation) with and without dark noise corrections in the phantom (a) and human forearm (b). The blue line represents a linear fitting of  $\ln[I(r)r^2]$  in the effective S-D ranges between the two vertical lines for extracting  $\mu_a$ . (c) and (d) Normalized  $K_s^2(r)$  (mean  $\pm$  standard deviation) after noise corrections in the phantom (c) and forearm (d). The blue line represents the model fitting of normalized  $K_s^2(r)$  in the S-D ranges between the two vertical black lines for extracting  $\alpha_{DB}$ . The phantom properties:  $\mu_a = 0.1 \text{ cm}^{-1}$ ,  $\mu_s' = 10.2 \text{ cm}^{-1}$ , and  $\alpha_{DB} = 1.28 \times 10^{-8} \text{ cm}^2/\text{s}$ . The human forearm properties:  $\mu_a = 0.25 \text{ cm}^{-1}$ ,  $\mu_s' = 5.3 \text{ cm}^{-1}$ , and  $\alpha_{DB} = 0.79 \times 10^{-8} \text{ cm}^2/\text{s}$ .

**Table 1. Empirically Determined Effective S-D Ranges**

	Tissue-simulating Phantoms (mm)	Human Forearm (mm)
Intensity $I(r)$	4.25–14.75	4.75 - 16.25
$K_s^2(r)$	2.75–13.75	4.75–14.75

### 3.2. Phantom test results

Figure 5 shows comparison results from tissue-simulating phantoms during ink titration (a to c) and temperature variation (d to f), measured by the scDCT and NIRS/DCS devices. During ink titration, significant correlations were observed between the scDCT and NIRS measurements of  $\mu_a$  changes (linear regression:  $R^2 > 0.99$ ,  $p < 10^{-4}$ ; a and c). Although  $\alpha_{DB}$  varied slightly during ink titration, no significant difference was observed between the scDCT and DCS measurements of  $\alpha_{DB}$  (paired t-test:  $p = 0.36$ ; b). The small variation in  $\alpha_{DB}$  might result from the influence of small room temperature variation on Intralipid particle motions in the phantom during the test.

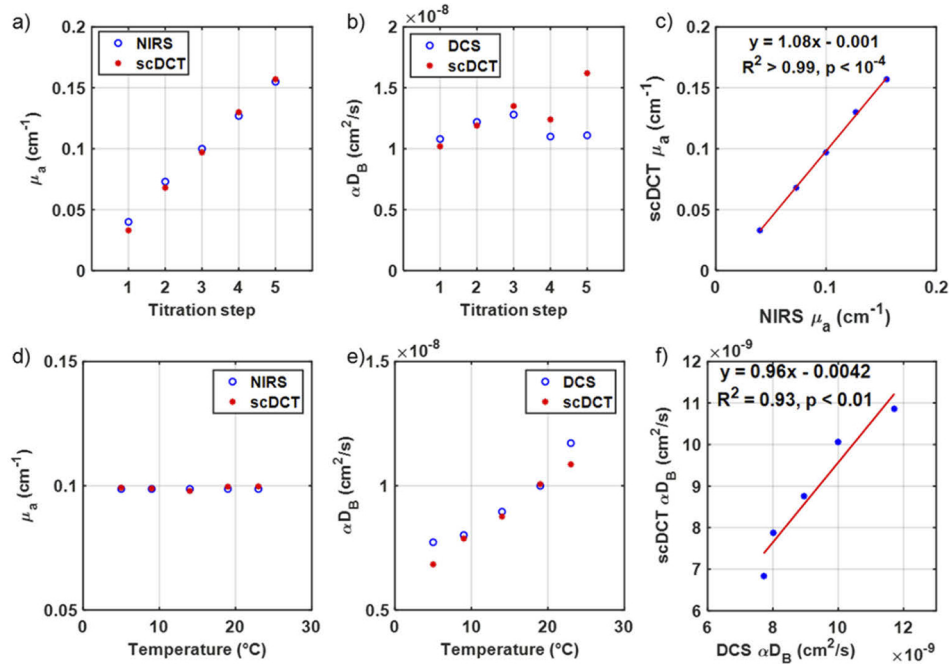
When creating a large temperature variation in the phantom, significant correlations were observed between the scDCT and DCS measurements of  $\alpha_{DB}$  changes (linear regression:  $R^2 = 0.93$ ,  $p < 0.01$ ; e and f). No significant differences were observed between the scDCT and NIRS measurements of  $\mu_a$  (paired t-test:  $p = 0.62$ ; d).

Table 2 lists all measurement results from tissue phantoms by the scDCT and NIRS/DCS devices. scDCT measurement errors were less than 16% (assuming NIRS/DCS as the gold standard), except one large outlier error in  $\alpha_{DB}$  (45.42%) at the last step of ink titration.

### 3.3. Human forearm test results

Figure 6 shows the results from five forearms, measured by the scDCT and NIRS/DCS devices. There was no significant difference between the mean values of  $\mu_a$  (paired t-test:  $p = 0.83$ ; a), measured by the two devices. A significant correlation was observed between scDCT and NIRS measurements of  $\mu_a$  (linear regression:  $R^2 = 0.88$ ,  $p = 0.018$ ; b). Similarly, there was





**Fig. 5. Results from Tissue-simulating Phantoms during Ink Titration (Top) and Temperature Variation (Bottom).** Ink titration: (a)  $\mu_a$ . (b)  $\alpha D_B$ . (c) Linear regression between the scDCT and NIRS measurements of  $\mu_a$ . Temperature variation: (d)  $\mu_a$ . (e)  $\alpha D_B$ . (f) Linear regression between the scDCT and DCS measurements of  $\alpha D_B$ .

**Table 2. Phantom Test Results**

	$\mu_a$ (cm <sup>-1</sup> )			$\alpha D_B$ ( $\times 10^{-8}$ cm <sup>2</sup> /s)		
	NIRS	scDCT	Error (%)	DCS	scDCT	Error (%)
Ink Titration	0.040	0.033	15.97	1.08	1.02	5.31
	0.073	0.068	6.21	1.22	1.19	3.05
	0.100	0.097	3.30	1.28	1.35	5.80
	0.127	0.130	2.29	1.10	1.24	13.23
	0.155	0.157	1.13	1.11	1.62	45.42
Temperature Variation	0.099	0.099	0.49	0.77	0.68	11.51
	0.099	0.099	0.20	0.80	0.79	1.72
	0.099	0.098	0.81	0.90	0.88	2.19
	0.099	0.100	0.91	1.00	1.01	0.67
	0.099	0.100	1.02	1.17	1.09	7.29

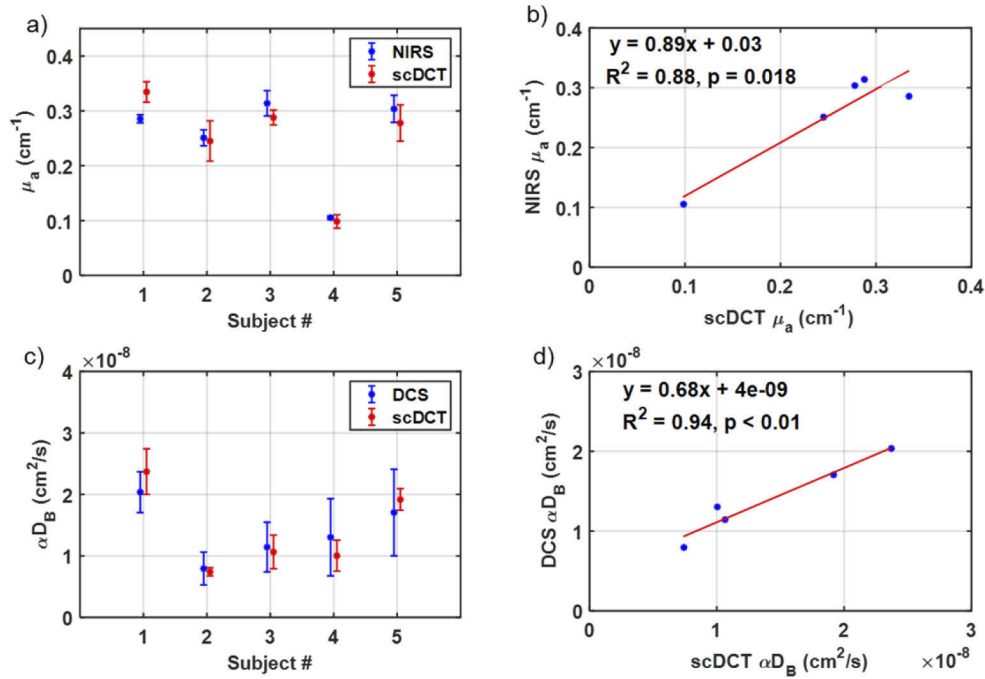


**Fig. 6. Results from Human Forearms.** (a)  $\mu_a$  (mean  $\pm$  standard deviation, over the measurement period of 10 seconds), measured by the scDCT and NIRS device. (b) Linear regression between the scDCT and NIRS measurements of  $\mu_a$ . (c)  $\alpha D_B$  (mean  $\pm$  standard deviation, over the measurement period of 10 seconds), measured by the scDCT and DCS devices. (d) Linear regression between the scDCT and DCS measurements of  $\alpha D_B$ .

no significant difference between the mean values of  $\alpha D_B$  (paired t-test:  $p = 0.85$ ; c), and a significant correlation was observed between the two measurements of  $\alpha D_B$  (linear regression:  $R^2 = 0.94$ ,  $p < 0.01$ ; d).

Table 3 lists all measurement results from human forearms by the scDCT and NIRS/DCS devices. Note that individual  $\alpha D_B$  was calculated using individual forearm  $\mu'_s$ , measured by the NIRS device. scDCT measurement errors were less than 23%, assuming NIRS/DCS as the gold standard.

**Table 3. Human Forearm Test Results (n = 5)**

$\mu_a$ (cm <sup>-1</sup> )			$\alpha D_B$ ( $\times 10^{-8}$ cm <sup>2</sup> /s)			$\mu'_s$ (cm <sup>-1</sup> )
NIRS	scDCT	Error (%)	DCS	scDCT	Error (%)	NIRS
0.286	0.335	17.13	2.04	2.37	16.39	2.49
0.251	0.245	2.32	0.79	0.74	6.639	5.26
0.314	0.288	8.28	1.14	1.06	6.87	6.03
0.105	0.098	6.50	1.30	1.00	22.95	4.65
0.304	0.278	8.50	1.71	1.92	12.38	4.21

#### 4. Discussion and conclusions

This study developed a new approach with two fitting steps to extract both  $\mu_a(\lambda)$  and  $BFI$  ( $\alpha D_B$ ) from innovative scDCT measurements of both light intensities and diffuse speckle contrasts at

multiple S-D distances. The assessment of  $\mu_a$  from the measured light intensities improved the accuracy of  $\alpha D_B$  calculations from the measured speckle contrasts. Moreover, knowledge of  $\mu_a(\lambda)$  at multiple wavelengths would enable quantification of tissue blood oxygenation [36,57,58]. The noncontact camera-based hardware of scDCT makes data acquisition easy and fast with a high sampling density, thus allowing for tomographic imaging [39–47]. Importantly, the fully noncontact measurements improve the versatility of scDCT in clinical applications where contact measurements may result in an infection risk or hemodynamic disruption on soft, vulnerable tissues.

The scDCT measurements with new fitting algorithms were examined in tissue-simulating phantoms with known optical properties and human forearms against standard NIRS/DCS measurements. We selected S-D distance ranges for light intensity and speckle contrast analyses based on satisfactory data fitting in  $\ln [I(\mathbf{r}) r^2]$  and  $K_s^2(\mathbf{r})$  to our models Eq. (4–6, and Fig. 4), respectively. As a result, the effective S-D ranges for light intensity and speckle contrast analyses were slightly different (Table 1). In the future, we may explore using the overlapped S-D range for both light intensity and speckle contrast analyses.

Phantom test results measured by the scDCT and NIRS/DCS devices were correlated and agreed well with expected values of  $\mu_a$  and  $\alpha D_B$  based on the phantom recipe over a relatively wide range of variations, which are commonly observed in biological tissues. Most of scDCT measurement errors in  $\mu_a$  and  $\alpha D_B$  were less than 16% (assuming NIRS/DCS as the gold standard), except one large outlier error in  $\alpha D_B$  (45.42%). Compared to phantom test results, *in vivo* test results in human forearms demonstrated slightly larger measurement discrepancies between the NIRS/DCS and scDCT measurements (up to 23%). These discrepancies might be partly attributed to temporal variation of  $\mu_a$  and  $\alpha D_B$  since the two measurements were taken sequentially. Tissue spatial heterogeneity might also contribute to the discrepancy as the two measurements covered different regions with different sizes/areas. In addition, NIRS/DCS probe-tissue contact pressure may result in tissue hemodynamic variations. The accuracies of our new fitting algorithms with scDCT measurements of multiple parameters are comparable to relevant study results. Up to 25% errors in fitting  $\mu_a$  and  $\alpha D_B$  were observed during DCS measurements at multiple S-D distances and multiple wavelengths and diffuse speckle contrast measurements at multiple S-D distances and multiple exposure times in manipulated tissue phantoms [51,52].

We note that use of a longer acquisition time for each measurement would improve SNR via temporal data averaging. However, it also impacts the temporal resolution of scDCT, especially when using multiple source positions for tomographic measurements. Moreover, possible physiological variations in the measured tissue over a long acquisition time may bias data collection.

In addition, we have also explored simultaneous extraction of  $\mu_a$ ,  $\mu'_s$  and  $\alpha D_B$  from scDCT measurements of light intensities and speckle contrasts at multiple S-D distances. The fitting accuracy was very sensitive to data quality and SNR (data are not shown). The crosstalk among  $\mu_a$ ,  $\mu'_s$  and  $\alpha D_B$  was also observed, as founded in previous studies [52,54,61]. To compare fitting sensitivities, we generated two noise-free reference curves (blue color):  $\ln [I(\mathbf{r}) r^2]$  in Fig. 7(a) and  $K_s^2(\mathbf{r})$  in Fig. 7(b), with the given parameters:  $\mu_a = 0.1 \text{ cm}^{-1}$ ,  $\mu'_s = 8 \text{ cm}^{-1}$ ,  $\alpha D_B = 1 \times 10^{-8} \text{ cm}^2/\text{s}$ ,  $r = 4$  to  $15 \text{ mm}$ . We then varied  $\mu_a$  from  $0.04 \text{ cm}^{-1}$  to  $0.16 \text{ cm}^{-1}$  to generate more testing curves. Apparently, variations in  $\ln [I(\mathbf{r}) r^2]$  resulting from  $\mu_a$  changes were much larger than in  $K_s^2(\mathbf{r})$ , indicating a better sensitivity of  $\ln [I(\mathbf{r}) r^2]$  to  $\mu_a$  changes (Fig. 7(a) and Fig. 7(b)). By contrast,  $K_s^2(\mathbf{r})$  signals are intrinsically sensitive to BFI. Therefore, our two-step fitting approach generated more robust results in  $\mu_a$  (by fitting  $\ln [I(\mathbf{r}) r^2]$ ) and BFI (by fitting  $K_s^2(\mathbf{r})$ ) than simultaneous fitting algorithms.

We recognize limitations of this pilot study in exploring new fitting algorithms for data analysis. The small number of subjects ( $n = 5$ ) impacts the study power, which will be addressed in future

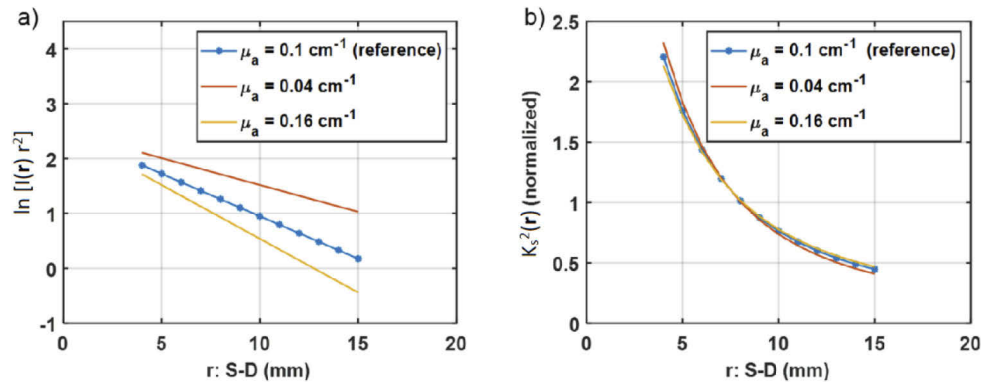


**Fig. 7. Comparison of Sensitivities in Fitting  $\mu_a$  Variations Using Light Intensities and Speckle Contrasts.** (a) A simulated reference curve of  $\ln[I(r)r^2]$  (blue line) generated with the given parameters ( $\mu_a = 0.1 \text{ cm}^{-1}$ ,  $\mu'_s = 8 \text{ cm}^{-1}$ ,  $\alpha D_B = 1 \times 10^{-8} \text{ cm}^2/\text{s}$ , S-D = 4 to 15 mm) and other simulated testing curves generated by varying  $\mu_a$  from  $0.04 \text{ cm}^{-1}$  to  $0.16 \text{ cm}^{-1}$ . (b) The simulated reference (blue line) and testing curves of  $K_s^2(r)$  generated with the same parameters as in (a).

studies. The effective S-D distances were determined manually based on the optimal fitting of experimental data to the models (Fig. 4 and Table 1). More experiments in a larger number of subjects are needed to generate a universally applicable method for automatic determination of effective S-D distances for data fittings. In this study,  $\mu'_s$  values were obtained from the phantom recipe or *in vivo* NIRS measurements. As mentioned earlier, simultaneous fitting of  $\mu_a$ ,  $\mu'_s$  and  $\alpha D_B$  using the current scDCT data generated unstable results with crosstalk. In the future, we will explore adding more wavelengths into the scDCT system and fit multi-wavelength and multi-distance data to extract all parameters simultaneously [51]. Finally, we will also explore 3D imaging of both blood flow and oxygenation distributions by developing a multiple-wavelength scDCT system.

**Funding.** National Institutes of Health (R01-EB028792, R01-HD101508, R01-RF1AG062480, R21-AR062356, R21-HD091118, R21-NS114771, R56-NS117587); Plastic Surgery Foundation; National Science Foundation (EPSCoR #1539068).

**Disclosures.** The authors declare no conflicts of interest.

**Data availability.** Data underlying the results presented in this paper are not publicly available at this time but may be obtained from the authors upon reasonable request.

## References

1. L. Dong, M. Kudrimoti, D. Irwin, L. Chen, S. Kumar, Y. Shang, C. Huang, E. L. Johnson, S. D. Stevens, B. J. Shelton, and G. Yu, "Diffuse optical measurements of head and neck tumor hemodynamics for early prediction of chemoradiation therapy outcomes," *J. Biomed. Opt.* **21**(8), 085004 (2016).
2. T. Durduran and A. G. Yodh, "Diffuse correlation spectroscopy for non-invasive, micro-vascular cerebral blood flow measurement," *NeuroImage* **85**(Pt 1), 51–63 (2014).
3. Y. Shang, K. Gurley, B. Symons, D. Long, R. Srikueta, L. J. Crofford, C. A. Peterson, and G. Yu, "Noninvasive optical characterization of muscle blood flow, oxygenation, and metabolism in women with fibromyalgia," *Arthritis Res. Ther.* **14**(6), R236 (2012).
4. K. Gurley, Y. Shang, and G. Yu, "Noninvasive optical quantification of absolute blood flow, blood oxygenation, and oxygen consumption rate in exercising skeletal muscle," *J. Biomed. Opt.* **17**(7), 0750101 (2012).
5. B. Henry, M. Zhao, Y. Shang, T. Uhl, D. T. Thomas, E. S. Xenos, S. P. Saha, and G. Yu, "Hybrid diffuse optical techniques for continuous hemodynamic measurement in gastrocnemius during plantar flexion exercise," *J. Biomed. Opt.* **20**(12), 125006 (2015).
6. L. Venkatraghavan, J. Poulblanc, S. Bharadwaj, O. Sobczyk, A. P. Crawley, D. M. Mandell, D. J. Mikulis, and J. A. Fisher, "Noninvasive measurement of cerebral blood flow under anesthesia using arterial spin labeling MRI: a pilot study," *J. Neurosurg. Anesthesiol.* **28**(4), 331–336 (2016).

7. O. U. Scremin, S. F. Figoni, K. Norman, A. M. Scremin, C. F. Kunkel, D. Opava-Rutter, E. D. Schmitter, A. Bert, and M. Mandelkern, "Preamputation evaluation of lower-limb skeletal muscle perfusion with H(2) (15)O positron emission tomography," *Am. J. Phys. Med. Rehabil.* **89**(6), 473–486 (2010).
8. H. A. Archer, N. Smailagic, C. John, R. B. Holmes, Y. Takwoingi, E. J. Coulthard, and S. Cullum, "Regional cerebral blood flow single photon emission computed tomography for detection of Frontotemporal dementia in people with suspected dementia," *Cochrane Database Syst Rev.* CD010896 (2015).
9. J. S. Meyer, N. Ishihara, V. D. Deshmukh, H. Naritomi, F. Sakai, M. C. Hsu, and P. Pollack, "Improved method for noninvasive measurement of regional cerebral blood flow by 133Xenon inhalation. Part I: description of method and normal values obtained in healthy volunteers," *Stroke* **9**(3), 195–205 (1978).
10. L. Chen, Y. Shang, E. Sipos, K. E. Saatman, G. Yu, and M. Toborek, "Novel experimental model for repeated forebrain ischemia-reperfusion," *J. Exp. Stroke Transl. Med.* **5**(1), 1–10 (2012).
11. Y. Shang, L. Chen, M. Toborek, and G. Yu, "Diffuse optical monitoring of repeated cerebral ischemia in mice," *Opt. Express* **19**(21), 20301–20315 (2011).
12. I. Blanco, P. Zirak, T. Dragojevic, C. Castellvi, T. Durduran, and C. Justicia, "Longitudinal, transcranial measurement of functional activation in the rat brain by diffuse correlation spectroscopy," *Neurophotonics* **4**(04), 1 (2017).
13. X. Zhang, "Instrumentation in Diffuse Optical Imaging," *Photonics* **1**(1), 9–32 (2014).
14. Q. Zhou, Y. Wang, L. Yi, Z. Tan, and Y. Jiang, "Multisensory interplay within human auditory cortex: new evidence from intraoperative optical imaging of intrinsic signal," *World Neurosurg.* **98**, 251–257 (2017).
15. M. Teichert and J. Bolz, "Simultaneous intrinsic signal imaging of auditory and visual cortex reveals profound effects of acute hearing loss on visual processing," *NeuroImage* **159**, 459–472 (2017).
16. C. Zhou, T. Shimazu, T. Durduran, J. Luckl, D. Y. Kimberg, G. Yu, X. H. Chen, J. A. Detre, A. G. Yodh, and J. H. Greenberg, "Acute functional recovery of cerebral blood flow after forebrain ischemia in rat," *J. Cereb. Blood Flow Metab.* **28**(7), 1275–1284 (2008).
17. T. Durduran, M. G. Burnett, G. Yu, C. Zhou, D. Furuya, A. G. Yodh, J. A. Detre, and J. H. Greenberg, "Spatiotemporal quantification of cerebral blood flow during functional activation in rat somatosensory cortex using laser-speckle flowmetry," *J. Cereb. Blood Flow Metab.* **24**(5), 518–525 (2004).
18. A. K. Dunn, "Laser Speckle Contrast Imaging of Cerebral Blood Flow," *Ann. Biomed. Eng.* **40**(2), 367–377 (2012).
19. C. Errico, J. Pierre, S. Pezet, Y. Desailly, Z. Lenkei, O. Couture, and M. Tanter, "Ultrafast ultrasound localization microscopy for deep super-resolution vascular imaging," *Nature* **527**(7579), 499–502 (2015).
20. E. Mace, G. Montaldo, B. F. Osmanski, I. Cohen, M. Fink, and M. Tanter, "Functional ultrasound imaging of the brain: theory and basic principles," *IEEE Trans. Ultrason., Ferroelect., Freq. Contr.* **60**(3), 492–506 (2013).
21. D. A. Boas and A. K. Dunn, "Laser speckle contrast imaging in biomedical optics," *J. Biomed. Opt.* **15**(1), 011109 (2010).
22. C. W. Lee, R. J. Cooper, and T. Austin, "Diffuse optical tomography to investigate the newborn brain," *Pediatr. Res.* **82**(3), 376–386 (2017).
23. E. M. W. Kooi, E. A. Verhagen, J. W. J. Elting, M. Czosnyka, T. Austin, F. Y. Wong, and M. J. H. Aries, "Measuring cerebrovascular autoregulation in preterm infants using near-infrared spectroscopy: an overview of the literature," *Expert Rev. Neurother.* **17**(8), 801–818 (2017).
24. A. M. Naidech, B. R. Bendok, M. L. Ault, and T. P. Bleck, "Monitoring with the Somanetics INVOS 5100C after aneurysmal subarachnoid hemorrhage," *Neurocrit. Care* **9**(3), 326–331 (2008).
25. E. E. Severdija, N. P. Vranken, S. Teerenstra, Y. M. Ganushchak, and P. W. Weerwind, "Impact of intraoperative events on cerebral tissue oximetry in patients undergoing cardiopulmonary bypass," *J Extra Corpor Technol* **47**(1), 32–37 (2015).
26. Y. Shang, R. Cheng, L. Dong, S. J. Ryan, S. P. Saha, and G. Yu, "Cerebral monitoring during carotid endarterectomy using near-infrared diffuse optical spectroscopies and electroencephalogram," *Phys. Med. Biol.* **56**(10), 3015–3032 (2011).
27. R. Cheng, Y. Shang, D. Hayes, S. P. Saha, and G. Yu, "Noninvasive optical evaluation of spontaneous low frequency oscillations in cerebral hemodynamics," *NeuroImage* **62**(3), 1445–1454 (2012).
28. R. Cheng, Y. Shang, S. Q. Wang, J. M. Evans, A. Rayapati, D. C. Randall, and G. Yu, "Near-infrared diffuse optical monitoring of cerebral blood flow and oxygenation for the prediction of vasovagal syncope," *J. Biomed. Opt.* **19**(1), 017001 (2014).
29. Y. Shang, T. Li, L. Chen, Y. Lin, M. Toborek, and G. Yu, "Extraction of diffuse correlation spectroscopy flow index by integration of Nth-order linear model with Monte Carlo simulation," *Appl. Phys. Lett.* **104**(19), 193703 (2014).
30. Y. Shang and G. Yu, "A Nth-order linear algorithm for extracting diffuse correlation spectroscopy blood flow indices in heterogeneous tissues," *Appl. Phys. Lett.* **105**(13), 133702 (2014).
31. E. M. Buckley, N. M. Cook, T. Durduran, M. N. Kim, C. Zhou, R. Choe, G. Yu, S. Shultz, C. M. Sehgal, D. J. Licht, P. H. Arger, M. E. Putt, H. Hurt, and A. G. Yodh, "Cerebral hemodynamics in preterm infants during positional intervention measured with diffuse correlation spectroscopy and transcranial Doppler ultrasound," *Opt. Express* **17**(15), 12571–12581 (2009).
32. T. Durduran, C. A. Zhou, E. M. Buckley, M. N. Kim, G. Yu, R. Choe, J. W. Gaynor, T. L. Spray, S. M. Durning, S. E. Mason, L. M. Montenegro, S. C. Nicolson, R. A. Zimmerman, M. E. Putt, J. J. Wang, J. H. Greenberg, J. A. Detre, A. G. Yodh, and D. J. Licht, "Optical measurement of cerebral hemodynamics and oxygen metabolism in neonates with congenital heart defects," *J. Biomed. Opt.* **15**(3), 037004 (2010).



33. M. N. Kim, T. Durduran, S. Frangos, B. L. Edlow, E. M. Buckley, H. E. Moss, C. Zhou, G. Yu, R. Choe, E. Maloney-Wilensky, R. L. Wolf, M. S. Grady, J. H. Greenberg, J. M. Levine, A. G. Yodh, J. A. Detre, and W. A. Kofke, "Noninvasive measurement of cerebral blood flow and blood oxygenation using near-infrared and diffuse correlation spectroscopies in critically brain-Injured adults," *Neurocrit. Care* **12**(2), 173–180 (2010).
34. D. A. Boas, L. E. Campbell, and A. G. Yodh, "Scattering and imaging with diffusing temporal field correlations," *Phys. Rev. Lett.* **75**(9), 1855–1858 (1995).
35. D. A. Boas and A. G. Yodh, "Spatially varying dynamical properties of turbid media probed with diffusing temporal light correlation," *J. Opt. Soc. Am. A* **14**(1), 192 (1997).
36. Y. Shang, Y. Zhao, R. Cheng, L. Dong, D. Irwin, and G. Yu, "Portable optical tissue flow oximeter based on diffuse correlation spectroscopy," *Opt. Lett.* **34**(22), 3556–3558 (2009).
37. J. Senarathna, A. Rege, N. Li, and N. V. Thakor, "Laser Speckle Contrast Imaging: theory, instrumentation and applications," *IEEE Rev. Biomed. Eng.* **6**, 99–110 (2013).
38. K. A. Morone, J. S. Neimat, A. W. Roe, and R. M. Friedman, "Review of functional and clinical relevance of intrinsic signal optical imaging in human brain mapping," *Neurophotonics* **4**(3), 031220 (2017).
39. C. Huang, D. Irwin, Y. Lin, Y. Shang, L. He, W. Kong, J. Luo, and G. Yu, "Speckle contrast diffuse correlation tomography of complex turbid medium flow," *Med. Phys.* **42**(7), 4000–4006 (2015).
40. C. Huang, D. Irwin, M. Zhao, Y. Shang, N. Agochukwu, L. Wong, and G. Yu, "Noncontact 3-D speckle contrast diffuse correlation tomography of tissue blood flow distribution," *IEEE Trans. Med. Imaging* **36**(10), 2068–2076 (2017).
41. S. Mazdeyasna, C. Huang, M. Zhao, N. B. Agochukwu, A. A. Bahrani, L. Wong, and G. Yu, "Noncontact speckle contrast diffuse correlation tomography of blood flow distributions in tissues with arbitrary geometries," *J. Biomed. Opt.* **23**(09), 1–9 (2018).
42. E. G. Abu Jawdeh, C. Huang, S. Mazdeyasna, L. Chen, L. Chen, H. S. Bada, and G. Yu, "Noncontact optical imaging of brain hemodynamics in preterm infants: a preliminary study," *Phys. Med. Biol.* **65**(24), 245009 (2020).
43. C. Huang, S. Mazdeyasna, L. Chen, E. G. Abu Jawdeh, H. S. Bada, K. E. Saatman, L. Chen, and G. Yu, "Noninvasive noncontact speckle contrast diffuse correlation tomography of cerebral blood flow in rats," *NeuroImage* **198**, 160–169 (2019).
44. A. Bonaroti, R. C. DeCoster, S. Mazdeyasna, C. Huang, G. Yu, and L. Wong, "The role of intraoperative laser speckle imaging in reducing postoperative complications in breast reconstruction," *Plast. Reconstr. Surg.* **144**(5), 933e–934e (2019).
45. C. Huang, S. Mazdeyasna, M. Mohtasebi, K. E. Saatman, Q. Cheng, G. Yu, and L. Chen, "Speckle contrast diffuse correlation tomography of cerebral blood flow in perinatal disease model of neonatal piglets," *J Biophotonics* **14**(4), e202000366 (2020).
46. M. Zhao, S. Mazdeyasna, C. Huang, N. Agochukwu-Nwubah, A. Bonaroti, L. Wong, and G. Yu, "Noncontact speckle contrast diffuse correlation tomography of blood flow distributions in burn wounds: a preliminary study," *Mil. Med.* **185**(Supplement\_1), 82–87 (2020).
47. S. Mazdeyasna, C. Huang, M. J. Zhao, A. R. Bonaroti, K. Saatman, L. Chen, E. G. Abu Jawdeh, H. S. Bada, B. A. Miller, L. Wong, and G. Q. Yu, "Noninvasive noncontact 3D optical imaging of blood flow distributions in animals and humans," *Ieee Int Symp Signal*, 129–134 (2018).
48. A. Duncan, J. H. Meek, M. Clemence, C. E. Elwell, L. Tysczuk, M. Cope, and D. T. Delpy, "Optical pathlength measurements on adult head, calf and forearm and the head of the newborn infant using phase resolved optical spectroscopy," *Phys. Med. Biol.* **40**(2), 295–304 (1995).
49. L. P. Safonova and A. B. Selivestrov, "[Manufacture of hydrogel-based phantoms of biological tissues and research into their optical properties]," *Biomed. Eng.* **47**(1), 2–6 (2013).
50. S. L. Jacques, "Optical properties of biological tissues: a review," *Phys. Med. Biol.* **58**(11), R37–R61 (2013).
51. D. Tamborini, P. Farzam, B. Zimmermann, K. C. Wu, D. A. Boas, and M. A. Franceschini, "Development and characterization of a multidistance and multiwavelength diffuse correlation spectroscopy system," *Neurophotonics* **5**(1), 011015 (2017).
52. J. Liu, H. Zhang, J. Lu, X. Ni, and Z. Shen, "Simultaneously extracting multiple parameters via multi-distance and multi-exposure diffuse speckle contrast analysis," *Biomed. Opt. Express* **8**(10), 4537–4550 (2017).
53. C. P. Valdes, H. M. Varma, A. K. Kristoffersen, T. Dragojevic, J. P. Culver, and T. Durduran, "Speckle contrast optical spectroscopy, a non-invasive, diffuse optical method for measuring microvascular blood flow in tissue," *Biomed. Opt. Express* **5**(8), 2769–2784 (2014).
54. P. Farzam and T. Durduran, "Multidistance diffuse correlation spectroscopy for simultaneous estimation of blood flow index and optical properties," *J. Biomed. Opt.* **20**(5), 055001 (2015).
55. T. Dragojevic, H. M. Varma, J. L. Hollmann, C. P. Valdes, J. P. Culver, C. Justicia, and T. Durduran, "High-density speckle contrast optical tomography (SCOT) for three dimensional tomographic imaging of the small animal brain," *NeuroImage* **153**, 283–292 (2017).
56. T. Dragojevic, E. E. Vidal Rosas, J. L. Hollmann, J. P. Culver, C. Justicia, and T. Durduran, "High-density speckle contrast optical tomography of cerebral blood flow response to functional stimuli in the rodent brain," *Neurophotonics* **6**(04), 1 (2019).
57. T. Li, Y. Lin, Y. Shang, L. He, C. Huang, M. Szabunio, and G. Yu, "Simultaneous measurement of deep tissue blood flow and oxygenation using noncontact diffuse correlation spectroscopy flow-oximeter," *Sci. Rep.* **3**(1), 1358 (2013).

58. X. Liu, Y. Gu, C. Huang, M. Zhao, Y. Cheng, E. G. A. Jawdeh, H. S. Bada, L. Chen, and G. Yu, "Simultaneous measurements of tissue blood flow and oxygenation using a wearable fiber-free optical sensor," *J. Biomed. Opt.* **26**(1), 012705 (2021).
59. A. M. Chiarelli, E. L. Maclin, K. A. Low, S. Fantini, M. Fabiani, and G. Gratton, "Low-resolution mapping of the effective attenuation coefficient of the human head: a multidistance approach applied to high-density optical recordings," *Neurophotonics* **4**(2), 021103 (2017).
60. H. Liu, D. A. Boas, Y. Zhang, A. G. Yodh, and B. Chance, "Determination of optical properties and blood oxygenation in tissue using continuous NIR light," *Phys. Med. Biol.* **40**(11), 1983–1993 (1995).
61. L. Dong, L. He, Y. Lin, Y. Shang, and G. Yu, "Simultaneously extracting multiple parameters via fitting one single autocorrelation function curve in diffuse correlation spectroscopy," *IEEE Trans. Biomed. Eng.* **60**(2), 361–368 (2013).
62. A. Rajaram, G. Bale, M. Kewin, L. B. Morrison, I. Tachtsidis, K. St Lawrence, and M. Diop, "Simultaneous monitoring of cerebral perfusion and cytochrome c oxidase by combining broadband near-infrared spectroscopy and diffuse correlation spectroscopy," *Biomed. Opt. Express* **9**(6), 2588–2603 (2018).
63. C. Huang, M. Seong, J. P. Morgan, S. Mazdeyasna, J. G. Kim, J. T. Hastings, and G. Yu, "Low-cost compact diffuse speckle contrast flowmeter using small laser diode and bare charge-coupled-device," *J. Biomed. Opt.* **21**(8), 080501 (2016).
64. D. A. Boas, "*Diffuse photon probes of structural and dynamical properties of turbid media: theory and biomedical applications*," (Citeseer, 1996).